

Lightweight Tracking Control for Computationally Constrained Aerial Systems with the Newton-Raphson Method

Evanns Morales-Cuadrado, Luke Baird, Yorai Wardi, and Samuel Coogan

Abstract—We investigate the performance of a lightweight tracking controller, based on a flow version of the Newton-Raphson method, applied to a miniature blimp and a mid-size quadrotor. This tracking technique has been shown to enjoy theoretical guarantees of performance and has been applied with success in simulation studies and on mobile robots with simple motion models. This paper investigates the technique through real-world flight experiments on aerial hardware platforms subject to realistic deployment and onboard computational constraints. The technique’s performance is assessed in comparison with the established control frameworks of feedback linearization for the blimp, and nonlinear model predictive control for both quadrotor and blimp. The performance metrics under consideration are (i) root mean square error of flight trajectories with respect to target trajectories, (ii) algorithms’ computation times, and (iii) CPU energy consumption associated with the control algorithms. The experimental findings show that the Newton-Raphson flow-based tracking controller achieves comparable or superior tracking performance to the baseline methods with substantially reduced computation time and energy expenditure.

Index Terms—Tracking control, quadrotor applications, blimp applications, model predictive control, Newton-Raphson flow, feedback linearization, barrier functions.

I. INTRODUCTION

THE past two decades have seen a significant shift in the nature of hardware research for trajectory control of aerial platforms like quadrotors. First, testing and verification of novel techniques relied heavily on numerical simulators, later transitioning to real-world deployments that depended on ground station computers and simplified models (e.g. dynamic reductions [1]) to achieve the high-frequency control required for stable flight. Today, powerful single-board computers (SBCs) have enabled research to shift toward onboard execution even for computationally intensive control methods [2]–[4]. These computers have allowed for the maturation of several control techniques, of which nonlinear model predictive control (NMPC) has emerged as the state-of-the-art for quadrotor control [5].

Advances in computing have also impacted controllers for other autonomous aerial vehicles. In the realm of blimp

research, older methods [6] were computationally limited to simplified linear models in order to perform model predictive control. More recent works, on the other hand, can implement NMPC with high-fidelity models [7]. Reinforcement learning-based controllers [8] that improve upon existing PID tracking controllers have also been implemented for blimps.

However, much of the state-of-the-art research has become dependent on exploiting powerful but relatively costly computing platforms. This renders them unrealistic for certain scenarios arising in applications. As noted in [4], it may be “impractical to run NMPC on some miniature aerial vehicles with a limited computational budget.” Furthermore, it was noted that even with such platforms, NMPC may fail to converge if the initial target reference and initial position of a quadrotor are too far apart.

This suggests an opening for exploration of effective tracking-control techniques that are computationally lightweight enough to not require top-of-the-line hardware for their implementation. Furthermore, similarly to NMPC, such techniques ought to be sufficiently general to be easily deployable on various hardware platforms with minimal alterations. Lastly, it is desirable for them to be capable of low-level control at high frequencies, be easily tunable, and offer strong theoretical guarantees.

The Newton-Raphson (NR) method is a tracking technique that meets all such criteria [9]. Based on an efficient algorithm, it can run effectively on computationally limited and inexpensive microcomputers such as the Raspberry Pi. Furthermore, while sharing a predictive element with NMPC, it performs only a one-instance lookahead at each iteration and does not require computations of optimal controls in the loop. In addition, it is backed by theoretical results and various simulation experiments that suggest a broad practical scope in the domain of autonomous vehicles [9]. It has only two tunable parameters, each with known ranges that have been empirically found to work across a wide range of systems. Moreover, its output predictor can be chosen from a broad class of functions, allowing for implementation across various platforms while accommodating constraints on model knowledge.

Prior work on the NR method has focused on its theoretical framework and simulation studies of various systems; see, e.g., [9], [10]. Laboratory results have been conducted on simple mobile robots with first-order models of motion. Our conference paper [11] was the first to conduct flight experiments

The NASA University Leadership Initiative (grant #80NSSC20M0161) provided funds to assist the authors with their research, but this article solely reflects the opinions and conclusions of its authors and not any NASA entity.

The authors are with the School of Electrical and Computer Engineering at the Georgia Institute of Technology, {egm, lbaird38, ywardi, sam.coogan}@gatech.edu. S. Coogan is also with the School of Civil and Environmental Engineering.

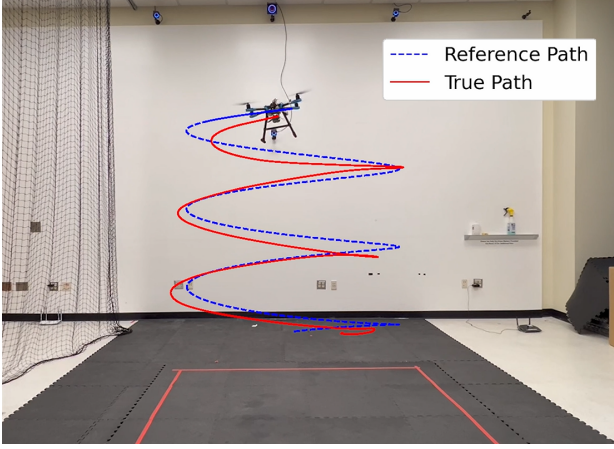


Fig. 1. Helix trajectory tracking with the Newton-Raphson method.

using the technique and test its tracking error performance against the native well-tuned PID tracking controller of the PX4 flight stack. In this paper we advance our investigations in several directions.

Firstly, in addition to the mid-size quadrotor, we extend our experiments to another aerial platform — the miniature blimp. The two types of Unmanned Aerial Vehicles (UAVs) are shown in Figure 5 and Figure 7.

Second, while the NR method has demonstrated remarkable robustness to predictors that prioritize computational speed over accuracy [11], new computational tools which we outline in Section IV-A allow us to perform highly accurate prediction at high speeds even under computational limitations.

Thirdly, due to these computational tools, we evaluate performance on a suite of trajectories and in comparison to well-tuned baseline frameworks that are well-established from the literature: feedback linearization (FBL) and NMPC. Lastly, we compare across three performance criteria: (i) root mean square error (RMSE) of the actuated trajectories from the given reference trajectories, (ii) average computation times, and (iii) CPU energy consumption.

The results¹ obtained from the blimp indicate that the FBL-based controller proposed in [7] is outperformed by the NR method on all three criteria. For the quadrotor, unlike many applications which depend on powerful onboard platforms such as the NVidia Jetson TX2 [3]–[5] or specialized micro-computers [2] for onboard control, we utilize a Raspberry Pi 4 Model B. This choice provides reasonable performance at a fraction of the price. Here, we find that the NR method is faster than NMPC, but performs with higher tracking error on most trajectories. However, for certain complex trajectories, NMPC fails to converge sufficiently fast, introducing undesirable flight characteristics, and even occasionally causing crashes. This phenomenon, described in detail in the sequel, suggests that the NR method holds out promise of complementing the established NMPC framework when applied to certain target trajectories.

¹Our code and video demonstrations can be found at: https://github.com/gtfactslab/MoralesCuadrado_TCST2025

The rest of the paper is organized as follows. Section II explains the NR tracking methodology and recounts relevant results. Section III and Section IV present experimental results for a miniature blimp and a mid-size quadrotor, respectively. Section V summarizes the obtained results and concludes the paper.

II. METHODOLOGY

This section describes the NR tracking control method for dynamical systems and provides a related literature survey. For detailed explanation and analysis please see [9], and simulation examples can be found in [10].

Consider the general feedback system depicted in Figure 2, where the reference signal $r(\cdot)$, the system's output $y(\cdot)$, the error signal $e(\cdot)$ and the input control to the plant, $u(\cdot)$, all have the same dimension m . The objective of the controller is to ensure that the output $y(\cdot)$ tracks the reference signal $r(\cdot)$ in a suitable sense. The tracking controller is based on the following three elements: (i) Fluid-flow version of the NR method for computing roots of algebraic functions, (ii) output prediction, and (iii) controller speedup.

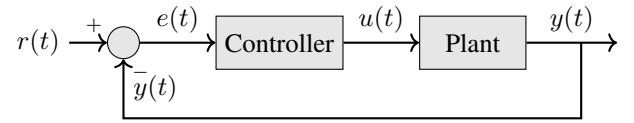


Fig. 2. Basic feedback control system.

We start the discussion with the following simple scenario in order to highlight the fundamental ideas underscoring the NR method. Assume that the combined plant and observer subsystem in Figure 2 is defined by a memoryless nonlinearity of the form

$$y(t) = g(u(t)), \quad (1)$$

where the function $g : \mathbb{R}^m \rightarrow \mathbb{R}^m$ is continuously differentiable. Suppose first that the target trajectory is a constant, namely $r(t) \equiv r$ for a given $r \in \mathbb{R}^m$. The tracking controller is defined as

$$\dot{u}(t) = \left(\frac{dg}{du}(u(t)) \right)^{-1} (r - g(u(t))). \quad (2)$$

Define the function $V : \mathbb{R}^m \rightarrow \mathbb{R}^+$ by

$$V(u) := \frac{1}{2} \|r - g(u)\|^2. \quad (3)$$

Under certain regularity assumptions [9], convergence of $u(t)$ to a root of the equation $g(u) = r$ is proven by taking the derivative $\dot{V}(u(t))$ in (3). To see this point, combine Eqs. (1) – (3) to derive

$$\dot{V}(u(t)) = -\langle r - g(u(t)), r - g(u(t)) \rangle = -2V(u(t)), \quad (4)$$

thereby establishing that $V(u(t))$ indeed is a Lyapunov function. In this case convergence of the output to the (constant) reference has the form

$$\lim_{t \rightarrow \infty} y(t) = r. \quad (5)$$

Next, we relax the assumption that $r(\cdot)$ is a constant and assume instead that $r(\cdot)$ is a bounded, continuous, and piecewise-continuously differentiable function of time t with bounded derivative $\dot{r}(t)$ over $t \in [0, \infty)$. We revise the definitions in Eqs. (2) and (3) by replacing r by $r(t)$, but the corresponding results in Eqs. (4) and (5) are no longer guaranteed, since $y(t)$ has to chase a time-dependent variable target $r(t)$. However, the following weaker conclusion is in force:

$$\limsup_{t \rightarrow \infty} \|r(t) - y(t)\| \leq \limsup_{t \rightarrow \infty} \|\dot{r}(t)\|. \quad (6)$$

Observe that (5) is the special case of (6) where $r(\cdot) \equiv r$, a constant.

A tightening of the right-hand side (RHS) in Eq. (6) can be obtained by scaling the RHS of the controller equation (2), with $r(t)$ replacing r , by a constant $\alpha > 1$, resulting in

$$\dot{u}(t) = \alpha \left(\frac{dg}{du}(u(t)) \right)^{-1} (r(t) - g(u(t))). \quad (7)$$

This scaling of the control law yields

$$\limsup_{t \rightarrow \infty} \|r(t) - y(t)\| \leq \alpha^{-1} \limsup_{t \rightarrow \infty} \|\dot{r}(t)\|. \quad (8)$$

The constant α acts as a controller-speedup factor, not gain, since Eq. (7) defines a dynamic control law actuating $\dot{u}(t)$ rather than $u(t)$.

The final stage of this discussion considers the most general case where the plant is modeled by

$$\dot{x}(t) = f(x(t), u(t)), \quad x(0) = x_0, \quad (9)$$

where $x(t) \in \mathbb{R}^n$ is the state variable whose initial value is $x_0 := x(0)$, and $u(t) \in \mathbb{R}^m$ is its control input. The output $y(t) \in \mathbb{R}^m$ is defined by

$$y(t) = h(x(t)). \quad (10)$$

The function $f : \mathbb{R}^n \times \mathbb{R}^m \rightarrow \mathbb{R}^n$ is assumed to have sufficient smoothness and boundedness properties for the existence of unique solutions of the differential equation (9) for $t \in [0, \infty)$, for every $u(\cdot)$ and x_0 in respective sets of interest. As for the function $h : \mathbb{R}^n \rightarrow \mathbb{R}^m$ in (10), it is assumed to be bounded, continuous, and piecewise-continuously differentiable with a bounded first derivative.

Observe that now $y(t)$ is not a function of $u(t)$, hence it is impossible to use Eq. (7) to define the controller. However, for a given $t \geq 0$ and $T > 0$, $x(t+T)$, hence $y(t+T)$ are functions of $x(t)$ and $\{u(\tau) : \tau \in [t, t+T]\}$. Thus, we wish to estimate the output $y(t+T)$ at time t , and generally the system does not have knowledge of the future inputs $u(\tau)$, $\tau \in (t, t+T]$. Therefore we resort to an output predictor denoted by $\tilde{y}(t+T)$, and we require that it be a function of $(x(t), u(t))$ but not of any future input. Formally, we have that

$$\tilde{y}(t+T) = g(x(t), u(t)) \quad (11)$$

for a continuous function $g : \mathbb{R}^n \times \mathbb{R}^m \rightarrow \mathbb{R}^m$, assumed to be continuously differentiable in (x, u) and whose partial Jacobian $\frac{\partial g}{\partial u}(x(t), u(t))$ is locally Lipschitz continuous in (x, u) . This suggests that a choice of smaller $T > 0$ likely would yield more-accurate predictions than larger T .

Given a fixed controller-speedup factor $\alpha > 1$ and prediction horizon $T > 0$, the NR method is defined by the following extension of (7),

$$\dot{u}(t) = \alpha \left(\frac{\partial g}{\partial u}(x(t), u(t)) \right)^{-1} (r(t+T) - g(x(t), u(t))). \quad (12)$$

The objective of this controller is to enable $\tilde{y}(t+T)$, not $y(t+T)$, to track the future input $r(t+T)$.²

By combining Eqs. (9) and (12), the closed-loop system can be viewed as a dynamical system with the compounded state variable $z := (x^\top, u^\top)^\top \in \mathbb{R}^n \times \mathbb{R}^m$. Unlike the situation with the aforementioned memoryless-plant systems, closed-loop stability cannot be taken for granted or easily ascertained. As a matter of fact, we made the following observations for almost every system we simulated throughout the research on the NR method: (i) *For every given $\alpha > 0$ there exists $\hat{T} > 0$ such that, for every $T \in (0, \hat{T})$, the closed-loop system is unstable.* This presents a conundrum: a small prediction horizon results in an instability of the closed-loop system, while a large T likely gives large prediction errors that translate to tracking errors of comparative magnitude. However, for various systems we noted the following phenomenon: (ii) *For every given $T > 0$ there exists $\hat{\alpha} > 0$ such that for every $\alpha > \hat{\alpha}$, the closed-loop system is stable.*

These two observations lead us to the following practical rule for selecting T and α : Start with $\alpha = 1$. Choose a small $T > 0$ associated with a related, sufficiently small prediction error if the closed-loop system is stable. Then choose $\alpha \geq 1$ large enough to ensure closed-loop system's stability. These computations of T and α typically have been determined *ad hoc* by trial and error on simulation experiments.

This procedure has worked well in just about every system we tested. Furthermore, we noticed dual benefits of increasing α : it stabilizes the closed-loop system and reduces the asymptotic tracking error when $r(\cdot)$ is time-dependent by guaranteeing the following extension of (8) for the predicted output \tilde{y} :

$$\begin{aligned} \limsup_{t \rightarrow \infty} \|r(t+T) - \tilde{y}(t+T)\| \\ \leq \alpha^{-1} \limsup_{t \rightarrow \infty} \|\dot{r}(t+T)\|. \end{aligned} \quad (13)$$

A more realistic characterization of asymptotic tracking can be obtained by replacing $\tilde{y}(t+T)$ by $y(t+T)$ in the left-hand side (LHS) of (13). Then

$$\begin{aligned} \limsup_{t \rightarrow \infty} \|r(t+T) - y(t+T)\| \\ \leq \limsup_{t \rightarrow \infty} \|y(t+T) - \tilde{y}(t+T)\| \\ + \alpha^{-1} \limsup_{t \rightarrow \infty} \|\dot{r}(t+T)\|. \end{aligned} \quad (14)$$

It is evident from this inequality that larger values of the controller's speedup factor α have no impact on the first term in the RHS of (14), which is the asymptotic prediction error.

²The future reference $r(t+T)$ is defined as the tracking-target at time $t+T$, regardless of how it is computed. For instance, in a simple case $r(\cdot)$ may be an exogenous process that is explicitly known to the system at the initial time $t_0 := 0$. In a more involved scenario, $r(t+T)$ may be a predicted value of an endogenous process of the system.

However, this situation can be resolved by the aforementioned procedure: Choosing a small prediction horizon $T > 0$ (assuming a faithful prediction model) typically results in a small asymptotic prediction error, and a large $\alpha > 0$ would stabilize the closed-loop system while reducing the second term in the RHS of (14). Thus, it seems to be possible to have the LHS of (14) be arbitrarily small by the choice of a small T and a large α . Of course certain conditions must be satisfied as discussed and analyzed in [9].

We close this section with a description of the predictor used throughout the paper. Recall that the state equation for the plant system is defined by (9) and the output equation is (10). Fix $T > 0$. For a given $t \geq 0$, consider the prediction interval $[t, t+T]$ over a time variable τ . First, we compute a predictor for the state variable $x(\tau)$, $\tau \in [t, t+T]$, denoted by $\xi(\tau)$. It is defined by the differential equation

$$\dot{\xi}(\tau) = f(\xi(\tau), u(t)), \quad \tau \in [t, t+T], \quad (15)$$

with the boundary condition $\xi(t) = x(t)$. Then we define the predicted value of $y(t)$ by the term $\tilde{y}(t+T) := h(\xi(t+T))$. In experiments, we use the forward Euler method for numerically integrating (15).

We observe that Eq. (15) has the initial condition $\xi(t) = x(t)$, and its input $u(\tau)$, $\tau \in (t, t+T]$ is frozen at its initial value, $u(t)$. This means that the predicted output $\tilde{y}(t+T)$ depends on $(x(t), u(t))$ but not on future inputs.

III. MINIATURE BLIMP

Miniature blimps are an aerial platform that pose interesting challenges for control. Blimps are constructed with a wide variety of actuation capabilities and envelope shapes, leading to a wide array of dynamic models. Unlike quadrotors, blimps' neutral buoyancy allows them to stay aloft without any actuation, and thus they can be flown at a far cheaper energy cost for long-term missions compared to quadrotors. Moreover, the dynamics of a blimp and a quadrotor are fundamentally different. Unlike the quadrotor, the blimp model considered in this paper has lightly damped zero dynamics in the rolling and pitching motions when input-output feedback linearized with positional outputs.

Several tracking control strategies have been proposed for miniature blimps. The paper [6] models a blimp as a simple chain of double integrators with time delay and tracks a desired yaw angle with model predictive control but is limited to only yaw tracking and ignores nonlinear dynamic effects. Sliding mode control has been demonstrated to achieve good tracking performance [12], but requires the selection of the correct manifold to project the dynamics onto and is computationally expensive.

In this work, we specifically consider a radially symmetric blimp with undermounted thrusters for lateral holonomic control [13], for which several further tracking controllers have been previously proposed. The paper [14] presents a controller that tracks a desired lateral velocity by tracking a fixed roll or pitch angle first in a multi-loop control architecture, however this method is specifically for velocity tracking. The paper [7] inverts the dynamics to derive an FBL-based

tracking controller. By including high-order control barrier functions (CBFs) to limit the roll and pitch angle—the residual zero dynamics—large roll and pitch angles are empirically mitigated.

A. Dynamic Model and Tracking Controllers for the Blimp

The radially symmetric blimp presented in [13] is modeled as a six-DOF underactuated system with holonomic lateral control. We briefly summarize the model as follows—a more complete representation is given in [7], [15]. Let $\nu_{b/n}^b = (v_{b/n}^b, \omega_{b/n}^b)$ represent translational and angular velocity in the body frame, and let $\eta_{b/n}^n = (p_{b/n}^n, \Theta_{b/n}^n)$ represent position in the world frame and orientation of the blimp relative to the world frame, respectively. We then define the state vector for the blimp as $x = (\nu_{b/n}^b, \eta_{b/n}^n) = (v_{b/n}^b, \omega_{b/n}^b, p_{b/n}^n, \Theta_{b/n}^n) \in \mathbb{R}^{12}$. The inputs are forces along each axis in the body frame and torque about the body frame z -axis, $u = [f_x f_y f_z \tau_z]^\top$.

The dynamics about the center of gravity (CG) are originally derived from a submarine physics model [16] and are given as

$$\begin{aligned} \dot{x} &= \begin{bmatrix} -(M^{CB})^{-1}C^{CB}(x) - (M^{CB})^{-1}D^{CB} & 0 \\ \text{diag}(R(\Theta), T(\Theta)) & 0 \end{bmatrix} \begin{bmatrix} \nu \\ \eta \end{bmatrix} \\ &\quad - (M^{CB})^{-1}G^{CB}(x) + (M^{CB})^{-1}u \\ y &= Wx \end{aligned} \quad (16)$$

where M^{CB} is the mass/inertia matrix, $C^{CB}(x)$ is the Coriolis-centripetal matrix, D^{CB} is the diagonal aerodynamic damping matrix, $R(\theta)$ is a rotation matrix, $T(\theta)$ is a transformation matrix, W is a binary matrix to select the position variables p_x, p_y, p_z, ψ , and the gravity vector is

$$G^{CB}(x) = - \begin{bmatrix} 0_{3 \times 1} \\ r_{g/b}^b \times f_{g/b}^b \end{bmatrix}, \quad f_g^b = (R_b^n(x))^{-1} \begin{bmatrix} 0 \\ 0 \\ f_{z,g}^n \end{bmatrix}$$

where $f_{z,g}^n$ is the constant downward force of gravity and $r_{g/b}^b = [0 \ 0 \ r_{z,g/b}^b]^\top$ is the position vector of the CG in the body frame, *i.e.* the vector from the center of buoyancy (CB) to the CG. Although translational acceleration due to gravity is zero due to the blimp's buoyancy, gravity induces non-zero restoring torque about the CB. The blimp and relevant coordinate frames are pictured in Figure 5.

In the case of the miniature blimp, we compare our proposed NR method against the FBL-based and NMPC control strategies developed in [7]. We utilize the same hardware, motion-capture software, and implementation of these miniature blimp controllers as in [7]. We briefly summarize these baseline controllers.

The FBL-based controller selects outputs $\sigma = [p_x p_y p_z \psi]^\top$ and inputs $u = [f_x f_y f_z \tau_z]^\top$. The blimp dynamics can be written in the control-affine form

$$\dot{\nu}_{b/n}^b = N(x)\nu_{b/n}^b + F(x) + Ku \quad (17)$$

with matrices $N(x)$, $F(x)$ and K given in [7, Equation 5–7].

Then, under appropriate geometric conditions, by [7, Theorem 1] the blimp is input-output feedback linearizable such

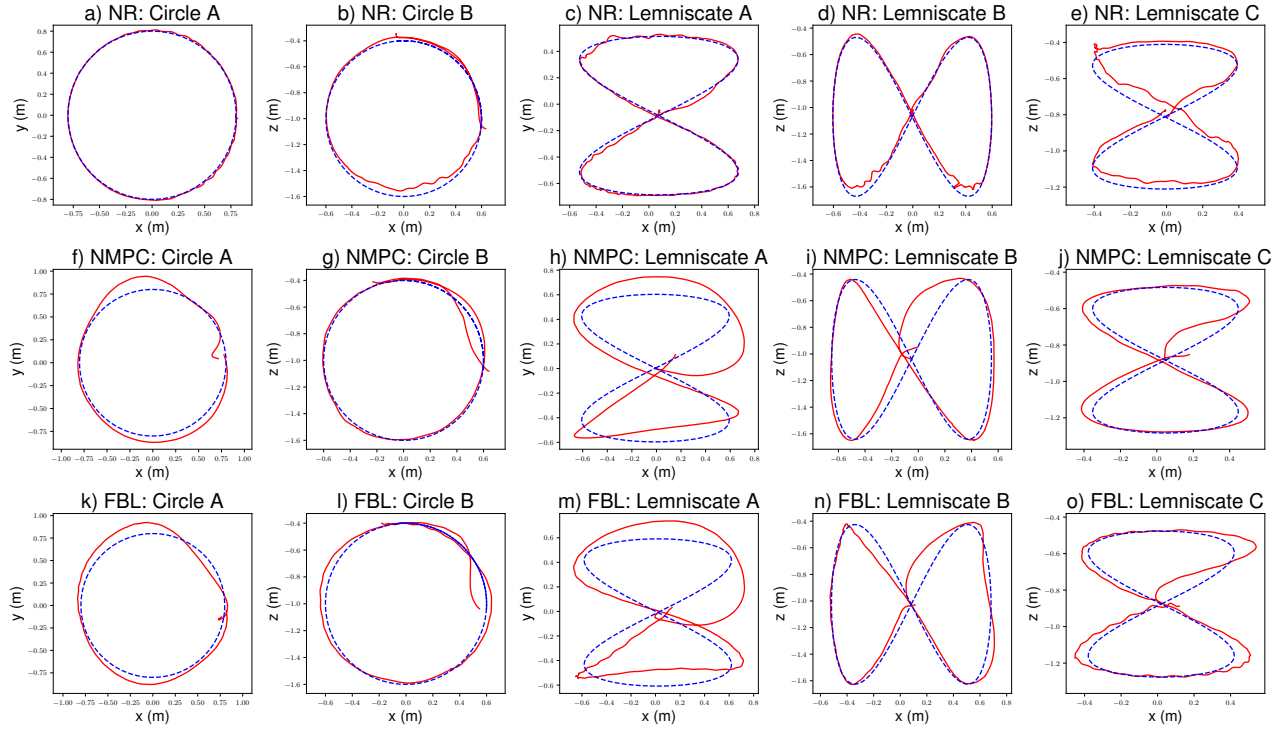


Fig. 3. Blimp: Comparison of five standard flight trajectories. Flight data in red, trajectory reference in blue. Rows from top to bottom are NR method, NMPC, and FBL-based controller.

that the second derivative of the outputs can be expressed in canonical form as

$$\ddot{\sigma} = a(x) + B(x)u := q \quad (18)$$

for state-dependent vector $a(x) \in \mathbb{R}^4$ and invertible matrix $B(x) \in \mathbb{R}^{4 \times 4}$.

This system is cast as a double integrator system with a virtual input q after performing a dynamic inversion of the form

$$u(x) = B^{-1}(x)(q - a(x)). \quad (19)$$

Now, given a reference trajectory $(r(t), \dot{r}(t), \ddot{r}(t))$ and corresponding error signal $e(t) := \sigma(t) - r(t)$, the feedback linearization controller tracks the reference via a proportional-derivative controller with feed-forward acceleration as the virtual input,

$$q = -k_1 e - k_2 \dot{e} + \ddot{r}. \quad (20)$$

Additionally, the feedback linearization controller is augmented with high-order CBFs that empirically mitigate the worst-case roll and pitch. For details on the implementation as a quadratic program, see [7].

The nonlinear model predictive controller that we compare to is also the baseline controller in [7]. Given the blimp dynamics in the form $\dot{x} = f(x, u)$, let $(r(t), \dot{r}(t))$ be the reference trajectory, and let $e(t) = \sigma(t) - r(t)$ be the tracking

error signal. After discretizing the dynamics with a zero-order hold, the optimization program

$$u_k^* = \underset{u_k}{\operatorname{argmin}} \sum_{j=k}^N e_j^\top Q e_j + u_j^\top R u_j \quad (21)$$

$$\text{s.t. } x_{j+1} = x_j + \Delta t f(x_j, u_j) \quad j = k, \dots, N-1$$

$$u_j \in \mathcal{U} \quad j = k, \dots, N-1$$

is repeatedly solved in CasADi [17], where Δt is the discretization step, Q and R are cost matrices, and \mathcal{U} represents the actuation limits.

B. Integral Control Barrier Functions for Smooth Actuator Saturation

Integral control barrier functions (I-CBFs) [18] are an extension of CBFs for dynamically defined control laws. I-CBFs can enforce forward invariance for both states and inputs by treating the input as an extended state variable. We utilize I-CBFs for smooth actuator saturation when utilizing the NR method. Denoting the right hand side of (12) by $\Psi(x(t), u(t), t)$, we modify the control law to

$$\dot{u}(t) = \Psi(x(t), u(t), t) + \eta(t), \quad (22)$$

where $\eta(t)$ is a minimal I-CBF intervention term that smoothly limits actuation. These developments yield a continuous-time NR dynamic control law with smooth input saturation to enhance flight safety. See [18], [19] for more information on I-CBFs and general CBFs, respectively.

Figure 6 displays the control inputs for the blimp in terms of forces and torque about the z-axis to track the horizontal

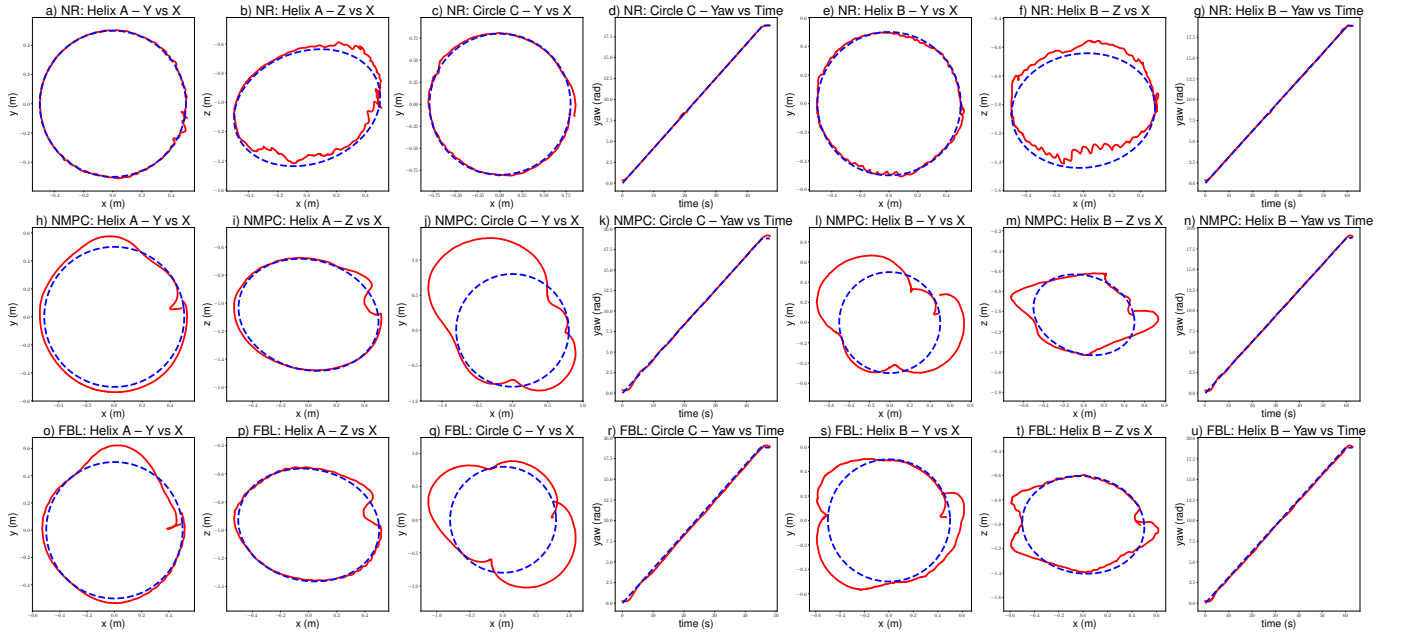


Fig. 4. Blimp: Comparison of three aggressive trajectories. Flight data in red, trajectory reference in blue. Rows from top to bottom are NR method, NMPC, and FBL-based controller.

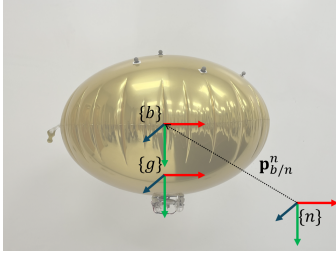


Fig. 5. The radially symmetric blimp with relevant coordinate frames.

circle trajectory. These are prescribed by the NR method and smoothly saturated with I-CBFs to keep them within the safe region, outlined by the red horizontal lines. Although the safe set of inputs should be forward invariant when utilizing barrier functions, hardware deployment creates conditions in which the forward invariance of the safe set of inputs may be temporarily violated. However, as shown in Figure 6, the inputs are always immediately pushed back into the safe region by the I-CBFs when this occurs.

C. Blimp Experimental Setup and Results

The blimp gondola is comprised of six counter-rotating motors (two vertical and four lateral), an inertial measurement unit (IMU), a motor board, and a Raspberry Pi Zero W. IMU data as well as motion-capture data from an OptiTrack system are streamed over a WiFi connection to a Dell Precision 5570 laptop with a 12th Gen Intel Core i7-12700H \times 20 CPU. The laptop first fuses IMU and motion-capture data to estimate states, and utilizes this information for control synthesis, from which appropriate motor commands are calculated. These

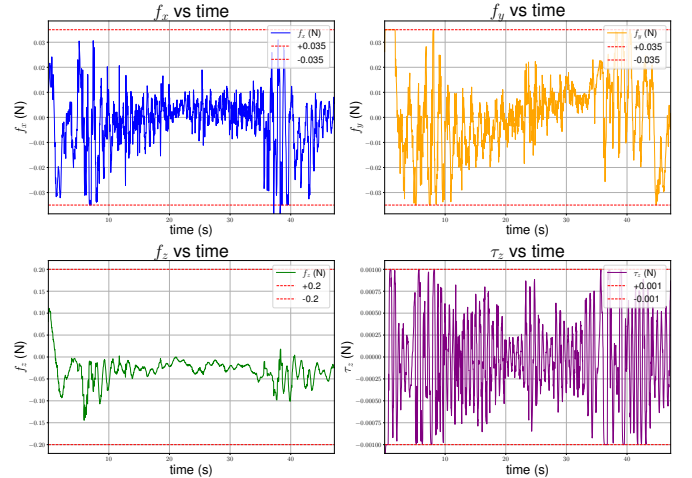


Fig. 6. Force and torque inputs from NR method smoothly saturated to within safe limits (red horizontal lines) via I-CBFs.

motor commands are sent to the motor board via a base station over a non-WiFi 2.4 GHz connection.

We compare the NR method, NMPC, and FBL-based controllers on the miniature blimp. The tracking results are plotted in Figures 3, 4 with error and computation time given in Tables I, II, respectively.

We selected five standard trajectories for the miniature blimp. These are Horizontal Circle (Circle A), Vertical Circle (Circle B), Horizontal Lemniscate (Lemniscate A), Vertical Short Lemniscate (Lemniscate B), Vertical Tall Lemniscate (Lemniscate C). We additionally selected three aggressive trajectories for the blimp: Regular Helix (Helix A), Yawing Helix (Helix B), and Yawing Horizontal Circle (Circle C).

For brevity, we sometimes shorten trajectory names or use the abbreviated names in parentheses (e.g., Horizontal Circle as Circle A).

TABLE I: Blimp - NR vs NMPC vs FBL RMSE

Trajectory	NR [m]	NMPC [m]	FBL [m]
Circle A	0.07866	0.14075	0.19332
Circle B	0.05137	0.10991	0.14255
Lemniscate A	0.10441	0.18517	0.22955
Lemniscate B	0.05389	0.10291	0.14565
Lemniscate C	0.05594	0.11793	0.13073
Helix A	0.07187	0.07732	0.11291
Helix B	0.08767	0.21534	0.22001
Circle C	0.10124	0.40327	0.38360

TABLE II: Blimp - Computation Time Comparison

Trajectory	NR [ms]	NMPC [ms]	FBL [ms]
Circle A	0.84 ± 0.046	58.67 ± 15.67	10.42 ± 9.69
Circle B	0.82 ± 0.031	51.47 ± 12.23	10.86 ± 10.43
Lemniscate A	0.82 ± 0.019	52.67 ± 12.49	10.51 ± 10.66
Lemniscate B	0.87 ± 0.23	54.18 ± 6.84	10.84 ± 10.12
Lemniscate C	0.86 ± 0.018	54.84 ± 11.93	10.72 ± 10.42
Helix A	0.94 ± 0.041	53.15 ± 6.78	9.89 ± 9.49
Helix B	0.95 ± 0.022	60.76 ± 12.78	10.27 ± 10.05
Circle C	0.96 ± 0.034	73.49 ± 20.92	10.18 ± 9.88

D. Blimp Analysis and Discussion

The NR method is an order of magnitude faster than the FBL-based controller, which is itself an order of magnitude faster than the NMPC controller, see Table II. We note that the FBL-based controller calls on CBFs to mitigate oscillations in its internal dynamics, which factor into its computation time.

Given a prescribed control update rate of 40 Hz, the NR and FBL-based controllers consistently meet the corresponding 25 ms deadline necessary for low-level control of our particular blimp platform. However, due to computational constraints, the NMPC controller does not meet its deadline and consequently tracking performance is degraded. Note that when performing a simulation with real-time computational requirements removed and a 3 s lookahead, the NMPC controller achieves the lowest tracking error, however this may not be realizable within realistic computational constraints.

We highlight a new advantage of the NR method. For both the FBL-based controller as well as NMPC to achieve competitive tracking performance, we found it was necessary to enhance them with reference trajectory derivative information. On the other hand, the NR method was only given the desired trajectory with no derivative information. Nevertheless, the RMSE for the NR method was 2–4 times less than the other controllers, as seen in Table I.

IV. QUADROTOR

Quadrotor research is led by work on small, agile indoor racing drones with significant onboard computing capabilities. In particular, quadrotors small enough to be classified as micro-unmanned aerial vehicles (MAVs) of a size between 0.1 m to 0.5 m in diagonal length and 0.1 kg to 0.5 kg of mass [20], [21] are very commonly used.



Fig. 7. The Holybro X500 V2 quadrotor used for hardware experiments. It is fitted with tracking markers, a radio receiver, and an on-board Raspberry Pi with ROS2 for control computations. The quadrotor weighs 2.1 kg, measures 0.6 m diagonally, and 0.25 m vertically.

While smaller quadrotors are desirable for upkeep and for multiagent research in small flight spaces, the primary reason for their expansive use lies in the physics of quadrotor flight. A quadrotor's translational motion is controlled by tilting its body, meaning rotational dynamics directly influence translational agility. Consequently, because angular acceleration is inversely proportional to the size of the quadrotor [21], MAVs feature prominently in modern research.

However, while less maneuverable, medium-sized and larger quadrotors have the inertia necessary to withstand unfavorable real-world weather conditions and can carry larger payloads [21], [22]. This makes research exploiting their strengths and addressing their limitations both useful for real-world deployment and less commonly addressed in work that focuses on small racing drones. In contrast to the dominant focus on MAV agility, our work investigates the complementary challenges posed by larger platforms. We begin with the challenges of computational constraints and limited vehicle agility, and seek to maximize trajectory speed and tracking accuracy despite these constraints. The quadrotor used in our flight experiments is seen in Figure 7.

A. Dynamic Model and Tracking Controllers for the Quadrotor

We model our quadrotor as a 9-state, 4-input system. We take the system state as

$$x = [p_x \ p_y \ p_z \ V_x \ V_y \ V_z \ \phi \ \theta \ \psi]^T \in \mathbb{R}^9 \quad (23)$$

where (p_x, p_y, p_z) is the system's 3D position in a fixed north, east, down (NED) world frame, (V_x, V_y, V_z) is the system's velocity within the frame, and (ϕ, θ, ψ) are Euler angles describing the orientation of the system within the same.

The system input is $u = [u_\tau, u_p, u_q, u_r]^T \in \mathbb{R}^4$ where u_τ is the net thrust through the quadrotor's body-frame z-axis and $\omega^b = (u_p, u_q, u_r)$ are angular body rates of the quadrotor. The nonlinear dynamics are

$$\begin{aligned} (\dot{p}_x, \dot{p}_y, \dot{p}_z) &= (V_x, V_y, V_z) \\ \dot{V}_x &= -\frac{u_\tau}{m} (s\phi s\psi + c\phi c\psi s\theta) \\ \dot{V}_y &= -\frac{u_\tau}{m} (c\phi s\psi s\theta - c\psi s\phi) \\ \dot{V}_z &= g - \frac{u_\tau}{m} (c\phi c\theta) \\ (\dot{\phi}, \dot{\theta}, \dot{\psi}) &= T \cdot \omega^b \end{aligned} \quad (24)$$

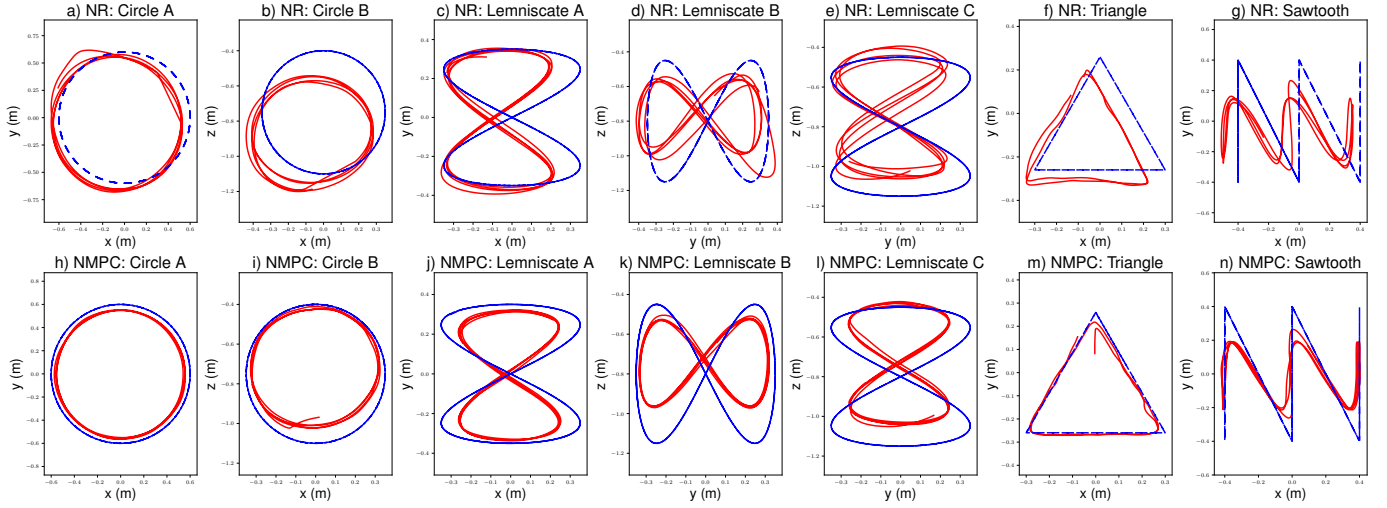


Fig. 8. Quadrotor: Flight data in red, trajectory reference in blue. Rows from top to bottom are NR method and NMPC.

where $c(\cdot)$, $s(\cdot)$, and $t(\cdot)$ are cosine, sine, and tangent, respectively, and T is the matrix for angular velocity transformations [23],

$$T = \begin{bmatrix} 1 & s\phi t\theta & c\phi t\theta \\ 0 & c\phi & -s\phi \\ 0 & \frac{s\phi}{c\theta} & \frac{c\phi}{c\theta} \end{bmatrix}.$$

For the quadrotor, we compare the NR method against a compiled NMPC algorithm built with the `acados` [24] fast embedded optimal control toolbox.

We seek to ensure the feasibility of forward Euler integration over the nonlinear quadrotor dynamics (24) for accurate output prediction that enables complex trajectory tracking with a minimum update rate of 100 Hz. This must be done despite the computational limitations of realistic deployment scenarios. To achieve this, we developed two equally effective solutions: (i) Compilation of the integration procedure in C via Cython and importing into Python as shared object, (ii) Just-in-Time (JIT) compilation via JAX. Calculation of the Jacobian is achieved via finite differences in the former, and via JIT-compiled forward-mode automatic differentiation in the latter. For the sake of consistency, all of our experiments use the latter implementation.³

B. Quadrotor Experimental Setup and Results

Leveraging the cascaded control architecture of the PX4 flight stack [25], we send rate control commands to the innermost loop of the stack. This control structure makes the system highly sensitive to small input variations, requiring continuous micro-adjustments. Consequently, tracking controllers deployed on such a system must publish commands at rates of at least 100 Hz to ensure flight stability.

In our hardware experiments, we use a Holybro X500 quadrotor equipped with a Pixhawk 6X flight controller as the flight management unit. Onboard control computations are performed using a Raspberry Pi 4 Model B transmitting

control commands to the flight controller via a serial connection. Communication between the Raspberry Pi and the flight controller is facilitated through the ROS 2 API available within the PX4 flight stack. The μ XRCE-DDS middleware serves as a bridge between PX4's native uORB topics and ROS 2 topics. For motion capture, we employ the OptiTrack system and use a relay to convert OptiTrack messages into visual odometry messages. These are subsequently fused with the flight controller's onboard sensor data via the flight stack's extended Kalman filter.

We again utilize the five standard trajectories from the Blimp experiments: Horizontal Circle (Circle A), Vertical Circle (Circle B), Horizontal Lemniscate (Lemniscate A), Vertical Short Lemniscate (Lemniscate B), and Vertical Tall Lemniscate (Lemniscate C). We also include the aggressive trajectories: Regular Helix (Helix A), Yawing Helix (Helix B), and Yawing Horizontal Circle (Circle C). Due to the higher maneuverability of quadrotors compared to blimps, we implement two additional aggressive trajectories: Sawtooth and Triangle. Figure 8 plots tracking results and provides a visual for the trajectories which can be plotted in two dimensions.

Comparative results of the five standard trajectories and the five aggressive trajectories are summarized in Tables III and IV, providing quantitative differences between the NR and NMPC approaches.

C. Quadrotor Analysis and Discussion

We note that the true flight paths are designed so that the quadrotor holds a hover position over the origin for five seconds before beginning each trajectory. At the end of each trajectory, the quadrotor is commanded to return to the origin and hover once again. This introduces a discontinuity in the reference that leads to a transient portion of flight, and we compare performance with and without this transient portion, as both NR and NMPC are known to have difficulties when the system state is far from the target.

³Implementation of both methods may be found in the github link provided.

TABLE III: Quadrotor - NR vs. NMPC, RMSE Comparison (Clipped vs. Non-Clipped Transients)

Trajectory	Clipped Transients		With Transients	
	NR [m]	NMPC [m]	NR [m]	NMPC [m]
Circle A	0.14849	0.13504	0.14401	0.25245
Circle B	0.14555	0.05069	0.14965	0.15162
Lemniscate A	0.12328	0.09402	0.12249	0.16343
Lemniscate B	0.15915	0.10721	0.15203	0.14905
Lemniscate C	0.15514	0.09938	0.14532	0.17329
Helix A	0.14879	0.08910	0.14867	0.27061
Helix B	0.19540	-	0.18851	-
Circle C	0.17398	-	0.17073	-
Sawtooth	0.17757	0.11540	0.16782	0.15924
Triangle	0.12852	0.12591	0.12822	0.14156

TABLE IV: Quadrotor - Average Computation Time Comparison for the NR method and NMPC

Trajectory	NR [ms]	NMPC [ms]
Circle A	4.00 \pm 1.32	9.84 \pm 5.48
Circle B	3.29 \pm 1.19	8.44 \pm 4.80
Lemniscate A	3.73 \pm 1.17	10.44 \pm 7.44
Lemniscate B	3.74 \pm 1.27	8.84 \pm 5.23
Lemniscate C	3.80 \pm 1.17	9.20 \pm 5.65
Helix A	3.82 \pm 1.16	11.36 \pm 8.06
Helix B	3.93 \pm 1.37	-
Circle C	3.87 \pm 1.20	-
Sawtooth	3.66 \pm 1.14	9.82 \pm 5.61
Triangle	3.87 \pm 1.03	8.83 \pm 4.98

If we clip these transient portions of flight to consider strictly the trajectory tracking abilities of the NMPC and NR methods, as seen in the “Clipped Transients” column of Table III, NMPC outperforms NR in terms of RMSE for all successful flights. However, NMPC struggled significantly with trajectories that included yawing references, leading to crashes and hardware damage when attempting Helix B and Circle C. As a result, we were unable to collect data for these trajectories with NMPC. Additionally, NMPC often displayed undesirable flight characteristics in the form of shaking behaviors, which can be seen in the video demonstrations. As will be discussed shortly, this shaking behavior is caused by the large computing requirements for NMPC.

Further, as noted previously, the tracking performance of both NMPC and NR can suffer when the initial position and initial target are far apart. When the transient flight portions are considered (“With Transients” column in Table III), the NR method outperforms NMPC on most trajectories.

Next, Table IV shows that computation time for the NR method is about three times faster than the NMPC algorithm. Further, NMPC’s computation time experienced large variations, with standard deviations being larger than the NR method’s for each trajectory, as well as varying significantly between trajectories. On the other hand, the NR method performed consistently with low standard deviations for each trajectory, as well as consistent average computation times across all trajectories.

In particular, NMPC’s computation time was lowest for trajectories with movements confined to a plane and noticeably increased as the complexity of trajectories increased to incorporate movement in a third dimension. This is seen in the Helix trajectory, which follows the same path as Circle A

TABLE V: Average CPU Energy Expenditure Comparison per Method on Blimp and Quadrotor

Method	Avg. CPU Energy Expenditure [μ J]
Blimp NR	$1.25 \times 10^4 \pm 4.29 \times 10^3$
Blimp MPC	$2.04 \times 10^5 \pm 3.80 \times 10^4$
Blimp FBL	$3.06 \times 10^4 \pm 2.22 \times 10^4$
Quad NR	$2.32 \times 10^4 \pm 8.15 \times 10^3$
Quad MPC	$2.81 \times 10^4 \pm 1.70 \times 10^4$

in the xy -plane, while periodically varying its altitude along the z -axis.

Helix B and Circle C differ from Helix A and Circle A by including yaw variation. The addition of a time-varying yaw reference increased computational times for NMPC such that the 100 Hz rate required for low-level control was no longer met. Consequently, each attempt to track the yawing trajectories led to crashes. Even on the standard trajectories, NMPC computation on average often took nearly the entire 10 ms allotted for each iteration, often taking longer due to the high variability. This inconsistency in command publishing rate prevented smooth flight and caused undesirable characteristics such as shaking behaviors, even for trajectories in which the clipped transient data showed superior RMSE tracking performance in comparison to the NR method.

Lastly, average energy expenditure across all methods for both quadrotor and blimp is shown in Table V. The NR method has the lowest CPU energy expenditure across all controllers used for both the blimp and quadrotor.

V. CONCLUSIONS

This work compares the proposed NR tracking control method against well-established alternatives from the literature on two aerial hardware platforms under realistic deployment and computational constraints. The comparison is based on three primary metrics: tracking accuracy, computation time, and CPU energy expenditure. The proposed controller is more generalizable than the FBL-based control method from the blimp literature, yet outperforms it across all three metrics. Compared to the more computationally demanding yet equally generalizable NMPC controller, the NR method demonstrates superior efficiency in computation time and CPU energy usage while maintaining competitive tracking accuracy across most trajectories and in some cases, achieving greater accuracy.

When given ample time, computational power, and agile hardware like micro-UAVs, NMPC achieves exceptional performance for aggressive trajectory tracking, as is well documented in the literature. However, its suitability may be limited in deployment scenarios where computational constraints prevent meeting real-time requirements for low-level control. As demonstrated in this study, the NR method provides a lightweight, adaptable, and theoretically grounded alternative, making it a viable choice for resource-constrained applications across a range of systems.

REFERENCES

- [1] M. Bangura and R. Mahony, “Real-time model predictive control for quadrotors,” *IFAC Proceedings Volumes*, vol. 47, no. 3, pp. 11773–11780, 2014. 19th IFAC World Congress.

- [2] M. Kamel, K. Alexis, M. Achteik, and R. Siegwart, “Fast nonlinear model predictive control for multicopter attitude tracking on $so(3)$,” in *2015 IEEE Conference on Control Applications (CCA)*, pp. 1160–1166, 2015.
- [3] F. Nan, S. Sun, P. Foehn, and D. Scaramuzza, “Nonlinear mpc for quadrotor fault-tolerant control,” 2022.
- [4] S. Sun, A. Romero, P. Foehn, E. Kaufmann, and D. Scaramuzza, “A comparative study of nonlinear mpc and differential-flatness-based control for quadrotor agile flight,” 2024.
- [5] D. Hanover, P. Foehn, S. Sun, E. Kaufmann, and D. Scaramuzza, “Performance, precision, and payloads: Adaptive nonlinear mpc for quadrotors,” *IEEE Robotics and Automation Letters*, vol. 7, p. 690–697, Apr. 2022.
- [6] H. Fukushima, K. Kon, Y. Hada, F. Matsuno, K. Kawabata, and H. Asama, “State-predictive control of an autonomous blimp in the presence of time delay and disturbance,” in *2007 IEEE International Conference on Control Applications*, pp. 188–193, IEEE, 2007.
- [7] M. Kasmalkar, L. Baird, and S. Coogan, “Feedback linearization of an underactuated miniature blimp with zero dynamics mitigation using high order control barrier functions,” *IEEE Control Systems Letters*, 2024.
- [8] Y. T. Liu, E. Price, M. J. Black, and A. Ahmad, “Deep residual reinforcement learning based autonomous blimp control,” in *2022 IEEE/RSJ International Conference on Intelligent Robots and Systems (IROS)*, pp. 12566–12573, IEEE, 2022.
- [9] Y. Wardi, C. Seatzu, J. Cortés, M. Egerstedt, S. Shivam, and I. Buckley, “Tracking control by the newton–raphson method with output prediction and controller speedup,” *International Journal of Robust and Nonlinear Control*, vol. 34, no. 1, pp. 397–422, 2024.
- [10] Y. Wardi, C. Seatzu, M. Egerstedt, and I. Buckley, “Performance regulation and tracking via lookahead simulation: Preliminary results and validation,” in *2017 IEEE 56th Annual Conference on Decision and Control (CDC)*, pp. 6462–6468, 2017.
- [11] E. Morales-Cuadrado, C. Llanes, Y. Wardi, and S. Coogan, “Newton-raphson flow for aggressive quadrotor tracking control,” in *2024 American Control Conference (ACC)*, pp. 3879–3884, 2024.
- [12] M. Wasim, A. Ali, M. A. Choudhry, I. Shaikh, and F. Saleem, “Robust design of sliding mode control for airship trajectory tracking with uncertainty and disturbance estimation,” *Journal of Systems Engineering and Electronics*, vol. 35, no. 1, pp. 242–258, 2024.
- [13] Q. Tao, M. Hou, and F. Zhang, “Modeling and identification of coupled translational and rotational motion of underactuated indoor miniature autonomous blimps,” in *16th International Conference on Control, Automation, Robotics and Vision*, pp. 339–344, IEEE, 2020.
- [14] Q. Tao, J. Tan, J. Cha, Y. Yuan, and F. Zhang, “Modeling and control of swing oscillation of underactuated indoor miniature autonomous blimps,” *Unmanned Systems*, vol. 9, no. 01, pp. 73–86, 2021.
- [15] Q. Tao, J. Wang, Z. Xu, T. X. Lin, Y. Yuan, and F. Zhang, “Swing-reducing flight control system for an underactuated indoor miniature autonomous blimp,” *IEEE/ASME Transactions on Mechatronics*, vol. 26, no. 4, pp. 1895–1904, 2021.
- [16] T. I. Fossen, *Handbook of marine craft hydrodynamics and motion control*. John Wiley & Sons, 2011.
- [17] J. Andersson, J. Gillis, G. Horn, J. Rawlings, and M. Diehl, “Casadi: a software framework for nonlinear optimization and optimal control,” *Mathematical Programming Computation*, vol. 11, 07 2018.
- [18] A. D. Ames, G. Notomista, Y. Wardi, and M. Egerstedt, “Integral control barrier functions for dynamically defined control laws,” *IEEE Control Systems Letters*, vol. 5, no. 3, pp. 887–892, 2021.
- [19] A. D. Ames, S. Coogan, M. Egerstedt, G. Notomista, K. Sreenath, and P. Tabuada, “Control barrier functions: Theory and applications,” in *2019 18th European Control Conference (ECC)*, pp. 3420–3431, 2019.
- [20] X. Liu, S. W. Chen, G. V. Nardari, C. Qu, F. Cladera, C. J. Taylor, and V. Kumar, “Challenges and opportunities for autonomous micro-uavs in precision agriculture,” *IEEE Micro*, vol. 42, no. 1, pp. 61–68, 2022.
- [21] A. Kushleyev, D. Mellinger, C. Powers, and V. Kumar, “Towards a swarm of agile micro quadrotors,” *Autonomous Robots*, vol. 35, no. 4, pp. 287–300, 2013.
- [22] C. Powers, D. Mellinger, and V. Kumar, *Quadrotor Kinematics and Dynamics*, pp. 307–328. Dordrecht: Springer Netherlands, 2015.
- [23] F. Sabatino, “Quadrotor control: modeling, nonlinear control design, and simulation,” Master’s thesis, KTH, Automatic Control, 2015.
- [24] R. Verschueren, G. Frison, D. Kouzoupis, J. Frey, N. van Duijkeren, A. Zanelli, B. Novoselnik, T. Albin, R. Quirynen, and M. Diehl, “acados: a modular open-source framework for fast embedded optimal control,” 2020.
- [25] PX4, “Controller diagrams.” https://docs.px4.io/main/en/flight_stack/controller_diagrams.html, 2023. [Online; accessed 2023-09-21].